

Excitation of Magnetosonic Waves in the Terrestrial Magnetosphere: Particle-in-cell Simulations

Kaijun Liu,¹ S. Peter Gary,¹ and Dan Winske¹

Kaijun Liu, Los Alamos National Laboratory, Los Alamos, NM 87545, USA.(kaijun@lanl.gov)

S. Peter Gary, Los Alamos National Laboratory, Los Alamos, NM 87545, USA.(pgary@lanl.gov)

Dan Winske, Los Alamos National Laboratory, Los Alamos, NM 87545, USA.(winske@lanl.gov)

¹Los Alamos National Laboratory, Los
Alamos, New Mexico, USA.

Abstract. Two-dimensional electromagnetic particle-in-cell simulations are performed to study the temporal development of an ion Bernstein instability driven by a proton velocity distribution with positive slope in the perpendicular velocity distribution $f_p(v_\perp)$, where \perp denotes directions perpendicular to the background magnetic field \mathbf{B}_0 . A subtracted Maxwellian distribution is first used to construct the positive slope in $f_p(v_\perp)$ and linear kinetic dispersion analysis is performed. The results of a simulation using such an initial proton distribution agree well with the linear kinetic analysis. The simulation results demonstrate that the ion Bernstein instability grows at propagation angles nearly perpendicular to \mathbf{B}_0 , and at frequencies close to the harmonics of the proton cyclotron frequency. The distribution in the simulation is further generalized to contain a proton shell with a finite thermal spread and a relatively cold ion background. The simulation results show that the presence of the cold background protons and the increase of the shell velocity shift the excited waves close to the cold plasma dispersion relation for magnetosonic waves, i.e., $\omega_r = kv_A$, where ω_r is the wave frequency, k is the wave number, and v_A is the Alfvén velocity. The general features of the simulated field fluctuations resemble observations of fast magnetosonic waves near the geomagnetic equator in the terrestrial magnetosphere. A test particle computation of energetic electrons interacting with the simulated electromagnetic fluctuations suggests that this growing mode may play an important role in the acceleration of radiation-belt relativistic electrons.

1. Introduction

Enhanced field fluctuation spectra with peaks at frequencies close to the proton cyclotron frequency and its harmonics up to the lower hybrid frequency have been observed near the geomagnetic equator of the terrestrial magnetosphere at radial distances between 2 and 8 R_E [Russell *et al.*, 1970; Perraut *et al.*, 1982; Santolík *et al.*, 2002]. The typical amplitude of the associated magnetic fluctuations is $0.03 \sim 0.2$ nT [Perraut *et al.*, 1982], which suggests $\delta B/B_0 \sim 10^{-4}$ (B_0 is the background geomagnetic field). The waves propagate nearly perpendicular to B_0 , are primarily confined within $2 \sim 3^\circ$ of the geomagnetic equator, and are mainly observed in the afternoon and premidnight sectors. Observations [Perraut *et al.*, 1982; Boardsen *et al.*, 1992; Meredith *et al.*, 2008] and theoretical studies [Gul’elmi *et al.*, 1975; McClements *et al.*, 1994; Chen *et al.*, 2010] suggest that the waves are driven by energetic protons at energies of tens keV which have ring-like distributions with $\partial f_p(v_\perp)/\partial v_\perp > 0$ ($f_p(v_\perp)$ is the perpendicular velocity distribution function).

These waves were first referred to as “equatorial noise” [Russell *et al.*, 1970], but more recently have been called “fast magnetosonic waves” because observations show that the wave magnetic field component is polarized along the background geomagnetic field [Perraut *et al.*, 1982] and the ratio of the electric field intensity to the magnetic field intensity is in good agreement with the theoretical values for fast magnetosonic waves at wave normal angles near 90° [Boardsen *et al.*, 1992]. These enhanced fluctuations are believed to play an important role in the transverse heating of thermal protons [Curtis, 1985; Horne *et al.*, 2000] and the acceleration of radiation-belt electrons [Horne and Thorne, 1998; Horne *et al.*, 2007; Shprits, 2009; Bortnik and Thorne, 2010].

Denton et al. [2010] provided further insight into these enhanced fluctuations. Using both Cluster observations in the plasma sheet boundary layer and linear kinetic dispersion theory, they demonstrated that the waves are excited by a ring-type property of the proton velocity distribution. They also found that the wave properties change significantly with the proton beta (β_p). At $\beta_p \ll 1$, these fluctuations are predominantly electrostatic, suggesting that these waves are more accurately described as ion Bernstein waves [Janhunen et al., 2003; Ashour-Abdalla et al., 2006]. As β_p approaches unity, the waves develop a strong electromagnetic component. The excited magnetic field fluctuations have components in both the perpendicular and parallel directions (with regard to \mathbf{B}_0), but the perpendicular fluctuations are larger. More interestingly, the parallel magnetic fluctuations δB_{\parallel} become dominant when β_p is further increased, which resembles the fluctuations referred to as fast magnetosonic waves that are observed near the geomagnetic equator in the terrestrial magnetosphere. These results have been confirmed by *Gary et al.* [2010], who further pointed out that the maximum instability growth rate decreases with increasing electron-to-proton temperature ratio.

Different with the situation in the plasma sheet boundary layer, magnetosonic waves in the inner magnetosphere are usually driven by a tenuous energetic (tens keV) proton velocity ring (relative density of several percent or less) in the presence of a cold dense background plasma (with electron and ion temperatures ~ 1 eV) [Perraut et al., 1982; Boardsen et al., 1992]. The ring velocity is $v_r \sim v_A$ where v_A is the Alfvén velocity. The ring generally has a significant thermal spread which corresponds to a thermal velocity on the order of one tenth of v_A [McClements et al., 1994; Horne et al., 2000]. Perraut et al. [1982] developed a simple theoretical model for the generation of magnetosonic

waves which includes a cold plasma background plus a cold proton ring. They found that when the relative density of the ring protons is small (2%), $v_r > v_A$ is required for instability and the excited waves approximately follow the cold plasma dispersion relation for magnetosonic waves, i.e., $\omega_r = kv_A$, where ω_r is the wave frequency and k is the wave number. However, $v_r > v_A$ is no longer a condition for instability for more intense proton rings (10%). The excited waves are shown to move away from the cold plasma dispersion relation for magnetosonic waves (Figure 17 of *Perraut et al.* [1982]) and are akin to the ion Bernstein waves studied in *Denton et al.* [2010] and *Gary et al.* [2010].

Although some simulation studies have addressed the ion Bernstein instability in the electrostatic limit [*Lee and Birdsall*, 1979; *Janhunen et al.*, 2003], no simulations have addressed the fully electromagnetic properties of this instability appropriate for the magnetosphere. The present study carries out two-dimensional (two spatial dimensions, but all three velocity components retained) electromagnetic particle-in-cell (PIC) simulations to investigate the properties of the ion Bernstein instability driven by proton distributions with $\partial f_p(v_\perp)/\partial v_\perp > 0$. The PIC code used is a reduced version of the three-dimensional PIC model in *Liu et al.* [2006] and has been successfully applied to the study of particle energization by oblique inertial Alfvén waves in the auroral region [*Seyler and Liu*, 2007]. In the present study, we first follow *Gary et al.* [2010] and use a subtracted Maxwellian distribution to drive the instability so that a close comparison of the simulation results with linear kinetic dispersion theory can be performed. Then the ion distribution is generalized in the simulation to include a proton shell with a finite thermal spread and a relatively cold ion background which has a Maxwellian distribution. The simulation results demonstrate that the ion Bernstein instability grows at propagation angles nearly

perpendicular to \mathbf{B}_0 , with a fluctuating field spectrum with peaks at frequencies close to the first few harmonics of the proton cyclotron frequency, in agreement with recent theory [Denton *et al.*, 2010; Gary *et al.*, 2010] and observations of fast magnetosonic waves. The results also show that the excited waves approach the cold plasma dispersion relation for magnetosonic waves as the relative density of the ring protons decreases and the ring velocity increases.

This paper is organized as follows: section 2 describes the linear kinetic dispersion analysis of the instability for a subtracted Maxwellian proton distribution; section 3 presents the simulation results of the instability for the subtracted Maxwellian proton distribution and the comparison with linear kinetic dispersion analysis; section 4 presents the simulation results of the instability for the generalized ion distribution; section 5 discusses the scattering of relativistic electrons by the simulated electromagnetic waves; and the conclusions are summarized in section 6. Throughout the paper, subscript p denotes proton quantities, and subscript e denotes electron quantities. The background magnetic field is $\mathbf{B}_0 = \hat{\mathbf{y}}B_0$, and the symbols \parallel and \perp denote directions relative to \mathbf{B}_0 . For the j th species or component, the plasma frequency is $\omega_j = \sqrt{n_j e_j^2 / \epsilon_0 m_j}$, the non-relativistic cyclotron frequency is $\Omega_j = e_j B_0 / m_j$ which contains the sign of the charge, and the thermal speed is $v_j = \sqrt{2k_B T_j / m_j}$. The Alfvén velocity is $v_A = B_0 / \sqrt{\mu_0 n_0 m_p}$, where n_0 is the unperturbed total plasma density. The ion inertial length is $\lambda_i = \sqrt{m_p / n_0 \mu_0 e^2}$.

2. Linear Kinetic Dispersion Theory

A simple subtracted Maxwellian distribution is first used to construct the positive slope in $f_p(v_\perp)$ in the present study because our linear kinetic dispersion code is based on

113 bi-Maxwellian velocity distributions [Gary, 1993]. The proton distribution is

$$114 \quad f_p(v) = f_1(v) - f_2(v), \quad (1)$$

115 with

$$116 \quad f_j(v) = \frac{n_j}{(\pi v_j^2)^{3/2}} \exp(-v^2/v_j^2). \quad (2)$$

117 Here $v^2 = v_{\parallel}^2 + v_{\perp}^2$, v_j is the j th species thermal speed (both are protons). This distribution
 118 is isotropic although non-Maxwellian. This simplifies the physics involved by excluding the
 119 possible development of the Alfvén cyclotron instability which can be driven by anisotropic
 120 protons [Gary, 1993]. We choose the dimensionless parameters to be $n_1/n_0 = 6.3$, $n_2/n_0 =$
 121 5.3 , $T_1/(m_p v_A^2) = 0.4$, $T_2/T_1 = 0.9$. Note that $n_2/n_1 < (T_2/T_1)^{3/2}$ is required to avoid
 122 negative values in $f_p(v)$. With these parameters, $\beta_p = (n_1 T_1 - n_2 T_2)/(B_0^2/2\mu_0) = 2(n_1 T_1 -$
 123 $n_2 T_2)/(n_0 m_p v_A^2) = 1.2$ and Figure 1a illustrates the proton velocity distribution $f_p(v_{\perp}, v_{\parallel})$
 124 in the v_{\parallel} - v_{\perp} coordinates. Electrons in the present study have a Maxwellian distribution
 125 and $T_e/T_1 = 0.01$.

126 In order to assess the amount of free energy available from the proton velocity distribu-
 127 tion used, we follow Janhunen *et al.* [2003] to define the free energy of a given distribution
 128 to be the kinetic energy of the original distribution minus the kinetic energy of the closest
 129 equilibrium distribution, assuming that the wave-particle interactions locally “level out”
 130 the positive slope in the original distribution and that the resulting distribution corre-
 131 sponds to the closest equilibrium distribution when the flattening procedure levels out
 132 the overall positive slope. In addition, we require the number of protons to be conserved
 133 ($4\pi \int_0^{\infty} v^2 f_p(v) dv = \text{constant}$) during the flattening procedure (Note the method in Jan-
 134 hunen *et al.* [2003] does not conserve the total number of particles, which is nonphysical).

With these assumptions, the original distribution used and its closest equilibrium distribution are shown in Figure 2 as the solid line and the dashed line, respectively. The free energy in this case is found to be only 0.35% of the total kinetic energy.

Linear kinetic dispersion theory for electromagnetic fluctuations in a homogeneous, magnetized, collisionless plasma is then applied to the instability analysis. The Cartesian coordinate system of the linear dispersion analysis [Gary, 1993] admits spatial variations in both the direction parallel to \mathbf{B}_0 (corresponding to y direction in the PIC simulations) and one direction perpendicular to the background field (corresponding to x direction in the PIC simulations), but no spatial variations in the other perpendicular direction (corresponding to z direction in the PIC simulations). So the wavevector is defined as $\mathbf{k} = k_\perp \hat{\mathbf{x}} + k_\parallel \hat{\mathbf{y}}$ and the complex frequency is $\omega = \omega_r + i\gamma$ where $\gamma > 0$ represents temporal growth of a fluctuating normal mode of the plasma.

Linear kinetic dispersion analysis for the given proton distribution using realistic proton-to-electron mass ratio ($m_p/m_e = 1836$) and $\omega_p/\Omega_p = 294$ has been reported by Gary *et al.* [2010]. They found that the ion Bernstein instability grows at frequencies near the proton cyclotron harmonics up to $\omega \approx 5\Omega_p$. The local maximum growth rate γ_{max} decreases as the harmonic number increases. For waves of $\omega \approx \Omega_p$, $\gamma_{max}/\Omega_p = 0.038$ at $k\lambda_i \approx 4.9$ and $\theta \approx 86.7^\circ$, where θ is the wave propagation angle with regard to \mathbf{B}_0 . For waves of $\omega \approx 2\Omega_p$, $\gamma_{max}/\Omega_p = 0.036$ at $k\lambda_i \approx 8.7$ and $\theta \approx 87.9^\circ$. In the present work, a reduced proton-to-electron mass ratio of 100 and a relatively small ω_p/Ω_p of 15 are used, consistent with the PIC simulations. Both observations and our simulations suggest that the instability saturates at very low level, which requires many simulation particles in order to achieve a reasonable signal-to-noise ratio in the simulation. Consequently, a

reduced proton-to-electron mass ratio and a relatively small ω_p/Ω_p are needed to enable a reasonably large time step. As we will show, choosing such reduced parameters does not change the essential physics, although they do slightly affect the properties of the ion Bernstein instability.

For the proton distribution shown in Figure 1a and the plasma parameters stated above, the ion Bernstein instability is found to grow at frequencies near the first two proton cyclotron harmonics ($\omega \approx \Omega_p, 2\Omega_p$). However, linear theory predicts that the growth of the instability at $\omega \approx 3\Omega_p, 4\Omega_p$, and $5\Omega_p$ is suppressed by the reduced proton-to-electron mass ratio and the relatively small ω_p/Ω_p used. The suppression of the higher harmonics is due to enhanced Landau damping from the electrons. The reduced parameters make the parallel wave electric field larger. They also shift the unstable waves slightly away from nearly perpendicular propagation so k_{\parallel} is larger and more electrons get into Landau resonance. Both factors would enhance the electron Landau damping, especially for higher harmonics. The growth rates as a function of $k\lambda_i$ and θ for waves near the first and the second proton cyclotron harmonics are displayed in the left panel and the right panel of Figure 3, respectively. The asterisk in each panel represents the location of the local maximum growth rate γ_{max} . For waves of $\omega \approx \Omega_p$, $\gamma_{max}/\Omega_p = 0.044$ at $k\lambda_i \approx 4.9$ and $\theta \approx 86.1^\circ$. For waves of $\omega \approx 2\Omega_p$, $\gamma_{max}/\Omega_p = 0.035$ at $k\lambda_i \approx 9.1$ and $\theta \approx 86.8^\circ$. The solid black contour line in each panel represents the contour of $\gamma/\Omega_p = 0.03$. The instability can grow over wide ranges of $k\lambda_i$ and θ with significant growth rates. Linear analysis also shows that the amplitude relations among electric and magnetic field components of these waves are $\delta E_x \gg \delta E_z \geq \delta E_y$ and $\delta B_z \geq \delta B_y \gg \delta B_x$, but the amplitude relation between δB_z and δB_y (δB_{\parallel}) changes with β_p quite significantly. The compressible component δB_{\parallel}

starts to dominate as β_p increases, in agreement of with the work of *Denton et al.* [2010].

Note that the instability has a large electrostatic component (δE_x) even at $\beta_p \sim 1$.

3. Simulation Results: Case I-Subtracted Maxwellian Distribution

A PIC simulation (Case I) is carried out for the subtracted Maxwellian distribution shown in Figure 1a and the simulation results are compared with the linear kinetic dispersion analysis in section 2. The two-dimensional simulation domain lies in the $x-y$ plane and the background magnetic field is in the y direction. Periodic boundary conditions are used in both dimensions. Due to the nearly perpendicular propagation of the instability, we choose $L_x = 9.6\lambda_i$, $N_x = 128$, $L_y = 64\lambda_i$, and $N_y = 64$. The present simulation has 48000 ions and 48000 electrons in each cell in order to achieve a reasonable signal-to-noise ratio. Consequently, a reduced proton-to-electron mass ratio ($m_p/m_e = 100$) and a relatively small $\omega_p/\Omega_p = 15$ are used to enable a reasonably large time step $\Delta t\Omega_p = 0.001$.

Figure 4 displays the time evolution of the energies in different electric and magnetic field components in the simulation. The panels from top to bottom are for E_x , E_y , E_z , B_x , B_y , and B_z , respectively. It is clear that $\delta E_x \gg \delta E_z \geq \delta E_y$ and $\delta B_z \geq \delta B_y \gg \delta B_x$, in agreement with the linear kinetic analysis results in section 2. The instability is weak and saturates at a very low level. The wave energy in the electric and magnetic fields at saturation is about 6×10^{-5} (normalized to $B_0^2/2\mu_0$), which is only 1% of the free energy estimated in Figure 2. So an exponential growth phase of the energy does not clearly stand out for some of the weakest field components, e.g., E_y . Nevertheless, the saturation levels shown by Figure 4 are reliable and physical, because another simulation with 9600 particles per cell produces the same saturation levels. The exponential growth phase of the magnetic energy of B_z estimates the growth rate of the instability to be $\gamma/\Omega_p \approx 0.03$.

This is slightly less than the growth rate predicted by the linear kinetic dispersion analysis based on the initial proton distribution. As we will show later, the interactions of the protons with the enhanced electromagnetic waves in the simulation gradually reduce the positive slope in the proton distribution, which naturally reduces the growth rate of the instability. Furthermore, note that the dominant electric field component is δE_x . It is mainly the electrostatic contribution, given the nearly perpendicular propagation of the instability. Nevertheless, $\delta E^2/(\delta B c)^2 \sim 0.1$, so most of the wave energy is still in the magnetic fluctuations, which is consistent with observations [Boardsen *et al.*, 1992].

Figure 5 displays the E_x fluctuations from the simulation at $t\Omega_p = 100$. The top panel shows the contour plot of E_x/cB_0 , while the bottom panel presents the spatial power spectrum of E_x/cB_0 . The two solid black contour lines in the bottom panel are the same ones in Figure 3 but are now plotted in the $k_\perp \lambda_i$ - $k_\parallel \lambda_i$ coordinates. They represent the contours of $\gamma/\Omega_p = 0.03$ given by linear kinetic dispersion theory for waves near the first two proton cyclotron harmonics. The lower left contour is for the first harmonic while the upper right contour is for the second harmonic. The regions of enhanced fluctuations are close to the two contours and reveal the growth of the waves near the first two proton cyclotron harmonics. This is further confirmed by Figure 6, which presents the temporal spectrum of E_x at $x = 4.8\lambda_i$ and $y = 32\lambda_i$ from $t\Omega_p = 80$ to $t\Omega_p = 160$. Spectral peaks at $\omega \approx \Omega_p, 2\Omega_p$ are clear, in agreement with the prediction of linear kinetic theory that the instability is unstable near the first two proton cyclotron harmonics. In addition, Figure 5 and Figure 6 suggest that the phase speed of the excited waves is much less than v_A so these waves do not follow the cold plasma dispersion relation for magnetosonic waves. This is consistent with the analysis of Perraut *et al.* [1982] that instability can occur even

if $v_r < v_A$ for intense proton rings and the excited waves move away from the cold plasma dispersion relation for magnetosonic waves in this case.

The proton distribution evolves with time in the simulation due to wave-particle interactions. The modification of the proton distribution is mainly due to E_x through ion gyroresonance with the enhanced waves. Figure 5 and Figure 6 suggest that the strongest waves in the simulation have $\omega_r \approx \Omega_p$, $k_\perp \lambda_i \approx 5$, and $k_\parallel \lambda_i \approx \pm 0.3$ (given the symmetry of the simulation, the system has waves propagating at both parallel and anti-parallel directions). The protons in cyclotron resonance with these waves are mainly the ones with $v_\parallel \approx 0$, as discussed in *Chen et al.* [2010]. In addition, *Kennel and Engelmann* [1966] found that a particle interacting with a single wave is constrained to move on a diffusion surface given by $(v_\parallel - \omega_r/k_\parallel)^2 + v_\perp^2 = \text{const.}$ In other words, particle energy is conserved in a reference frame moving at the parallel phase velocity of the wave. The proton velocity distribution at $t\Omega_p = 160$ from the simulation is displayed in Figure 1b. Figure 1c shows the difference between Figure 1a and Figure 1b and highlights the change of the proton distribution from $t\Omega_p = 0$ to $t\Omega_p = 160$. The two dashed lines in Figure 1c represent the diffusion surfaces for protons of $v_\parallel = 0$ and $v_\perp/v_A = 0.8$ interacting with the strongest waves of $k_\parallel \lambda_i \approx 0.3$ and $k_\parallel \lambda_i \approx -0.3$, respectively. Protons of $v_\parallel \approx 0$ are clearly scattered from a region near $v_\parallel/v_A = 0.6$ toward $v_\parallel = 0$, following the direction of the diffusion surfaces. To further demonstrate the change of the proton distribution, $f_p(v_\perp)$ for protons of $|v_\parallel|/v_A \leq 0.01$ at $t\Omega_p = 160$ is calculated from the simulation and shown as the dash-dotted line in Figure 2. The positive slope in $f_p(v_\perp)$ (for protons with $v_\parallel \approx 0$) has been reduced by the development of the instability.

4. Simulation Results: Case II-Generalized Proton Distribution

Magnetosonic waves in the inner magnetosphere are usually driven by a tenuous energetic proton velocity ring in the presence of a relatively cold dense background plasma [Perraut *et al.*, 1982; Boardsen *et al.*, 1992]. The presence of the background plasma is important and affects the properties of the instability. This section presents the results of another PIC simulation (Case II) which includes 90% of relatively cold background protons. In this simulation, we generalize the subtracted Maxwellian proton distribution in section 3 to a distribution composed of a proton shell with a finite thermal spread and a relatively cold ion background,

$$f_p(v) = \frac{n_s}{A} \exp[-(v - v_s)^2/v_{sth}^2] + \frac{n_b}{(\pi v_{bth}^2)^{3/2}} \exp[-(v)^2/v_{bth}^2], \quad (3)$$

where n_s , v_{sth} , v_s , n_b , and v_{bth} are the density of the shell protons, the thermal spread of the shell protons, the shell velocity, the density of the background ions, the thermal velocity of the background ions, respectively, and $A = \pi^{3/2} v_{sth} (v_{sth}^2 + 2v_s^2) [1 + \text{erf}(v_s/v_{sth})] + 2\pi v_s v_{sth}^2 \exp(-v_s^2/v_{sth}^2)$ is the normalization factor (erf is the error function). Here a velocity shell is used instead of a velocity ring. The reason is similar as discussed in section 2 that using an isotropic distribution simplifies the physics involved by excluding the possible development of the Alfvén cyclotron instability. The advantage of this generalized distribution over the subtracted Maxwellian distribution is that we can now freely adjust v_s while the thermal spread of the proton shell is unaffected. However, a linear kinetic dispersion code for such a distribution is currently not available so the simulation results cannot yet be compared against linear kinetic theory.

The subtracted Maxwellian distribution used in Case I is indeed close to a proton shell with $v_s/v_A = 0.8$ and $v_{sth}/v_A = 0.7$. If we choose the dimensionless parameters in equation

3 to be $n_s/n_0 = 1$ (so $n_b/n_0 = 0$), $v_{sth}/v_A = 0.7$, and $v_s/v_A = 0.8$, the resulting proton distribution can be shown to be close to the subtracted Maxwellian distribution (the solid line) shown in Figure 2. As expected, a simulation using such a proton shell as the initial proton distribution (all other parameters are the same as in section 3) produces very similar results (not shown).

In the simulation of Case II, we have $n_s/n_0 = 0.1$ (so $n_b/n_0 = 0.9$), $v_{sth}/v_A = 0.45$, $v_s/v_A = 2.0$, and $v_{bth}/v_A = 0.045$ (which corresponds to a temperature of 5 eV if $v_s/v_A = 2.0$ corresponds to 10 keV). The resulting proton distribution from equation (3) is shown in Figure 7 as the solid line. It is also displayed in the $v_{||}$ - v_{\perp} coordinates by Figure 8a. This distribution resembles the proton distribution used in *Horne et al.* [2000] except that n_s is slightly larger here to drive the instability more strongly to facilitate the development of the instability in the PIC simulation. For such a proton distribution, the simple theoretical model in *Perraut et al.* [1982] suggests that the excited waves would approach the cold plasma dispersion relation for magnetosonic waves since v_s is large and n_s is relatively small. Accordingly, we choose $L_x = 12.8\lambda_i$, $N_x = 128$, $L_y = 384\lambda_i$, and $N_y = 128$ (also through trial and error). The simulation has 14400 energetic shell protons, 14400 background protons and 14400 electrons in each cell. Same as Case I, a reduced proton-to-electron mass ratio ($m_p/m_e = 100$) and a relatively small $\omega_p/\Omega_p = 15$ are used to enable a reasonably large time step $\Delta t\Omega_p = 0.001$. The electrons in Case II follow a Maxwellian distribution and have the same temperature as the background ions.

Figure 9 displays the time evolution of the energies in different electric and magnetic field components in the simulation. Same as Figure 4, the panels from top to bottom are for E_x , E_y , E_z , B_x , B_y , and B_z , respectively. While δE_x still dominates among the electric

field components, the compressible magnetic component δB_{\parallel} (δB_y) dominates among the magnetic field components. This is consistent with the magnetosonic wave observations in the inner magnetosphere that the wave magnetic field component is polarized along the background geomagnetic field [Perraut *et al.*, 1982]. As in Case I, most of the wave energy is in the magnetic fluctuations ($\delta E^2/(\delta B c)^2 \sim 0.1$). The exponential growth phase of the magnetic energy of B_y estimates the growth rate of the instability to be $\gamma/\Omega_p \approx 0.07$, which is larger than the growth rate in Case I as v_s is larger in Case II.

The E_x fluctuations from the simulation at $t\Omega_p = 70$ are shown in Figure 10. The top panel shows the contour plot of E_x/cB_0 and the bottom panel presents its spatial power spectrum. The strongest wave in the simulation is at $k_x\lambda_i \approx 3.5$, and $k_y\lambda_i \approx 0.3$, which corresponds to a propagation angle of 85° . Figure 11 presents the frequency spectrum of E_x at $x = 6.4\lambda_i$ and $y = 192\lambda_i$ from $t\Omega_p = 0$ to $t\Omega_p = 100$. It is clear that the unstable harmonics have shifted to the third, the fourth and the fifth proton cyclotron harmonics. Figure 11 also shows that the fourth harmonic is the strongest one and suggests that it corresponds to the strongest wave at $k_x\lambda_i \approx 3.5$, and $k_y\lambda_i \approx 0.3$ in Figure 10. If so, the corresponding phase speed of this wave is $\omega/k \approx 1.1v_A$. Therefore, the excited waves are close to the cold plasma dispersion relation for magnetosonic waves as suggested by the simple theoretical model in Perraut *et al.* [1982]. Due to the contribution of the energetic shell protons, the overall plasma is not exactly cold. This might have caused the phase velocity to be slightly larger than the Alfvén velocity.

Similar to Case I, the proton distribution evolves with time in Case II due to wave-particle interactions. Figure 8b displays the proton velocity distribution $f_p(v_{\perp}, v_{\parallel})$ at $t\Omega_p = 100$. The change of the shell proton distribution from $t\Omega_p = 0$ to $t\Omega_p = 100$ is

shown in Figure 8c. As discussed above, the strongest waves in Case II have $\omega_r \approx 4\Omega_p$, $k_\perp \lambda_i \approx 3.5$, and $k_\parallel \lambda_i \approx \pm 0.3$ (the system has waves propagating at both parallel and anti-parallel directions due to the symmetry of the simulation). The two dashed lines in Figure 8c represent the diffusion surfaces for protons of $v_\parallel = 0$ and $v_\perp/v_A = 2$ interacting with the strongest waves of $k_\parallel \lambda_i \approx 0.3$ and $k_\parallel \lambda_i \approx -0.3$, respectively. Protons of $v_\parallel \approx 0$ are scattered from a region near $v_\parallel/v_A = 2$ toward $v_\parallel \sim 1$, following the diffusion surfaces. In addition, $f_p(v_\perp)$ for protons of $|v_\parallel|/v_A \leq 0.02$ at $t\Omega_p = 100$ is calculated from the simulation and shown as the dash-dotted line in Figure 7. The trough in $f_p(v_\perp)$ (for protons with $v_\parallel \approx 0$) has been filled up and the positive slope has disappeared.

5. Scattering of Relativistic Electrons

Fast magnetosonic waves in magnetosphere are believed to play an important role in scattering the relativistic radiation-belt electrons [Horne and Thorne, 1998; Horne et al., 2007; Shprits, 2009; Bortnik and Thorne, 2010]. Like whistler waves, they not only pitch-angle scatter but also accelerate the relativistic electrons. Wave-particle interactions in the radiation belts have been usually studied in terms of quasi-linear theory [Kennel and Engelmann, 1966; Lerche, 1968]. According to quasi-linear theory, the scattering of electrons by electromagnetic waves is described by a Fokker-Planck diffusion equation [Summers, 2005],

$$\begin{aligned} \frac{\partial f}{\partial t} = & \frac{1}{\sin \alpha} \frac{\partial}{\partial \alpha} \left(D_{\alpha\alpha} \sin \alpha \frac{\partial f}{\partial \alpha} \right) + \frac{1}{\sin \alpha} \frac{\partial}{\partial \alpha} \left(D_{\alpha p} \sin \alpha \frac{\partial f}{\partial p} \right) \\ & + \frac{1}{p^2} \frac{\partial}{\partial p} \left(p^2 D_{p\alpha} \frac{\partial f}{\partial \alpha} \right) + \frac{1}{p^2} \frac{\partial}{\partial p} \left(p^2 D_{pp} \frac{\partial f}{\partial p} \right), \end{aligned} \quad (4)$$

where f is the spatially uniform, zeroth-order, gyrophase-averaged electron distribution function, t is time, α is pitch angle, $p = |\mathbf{p}| = |\gamma m_e \mathbf{v}|$ is the electron momentum ($\gamma =$

1/ $\sqrt{1 - v^2/c^2}$ is the Lorentz factor), $D_{\alpha\alpha}$ is the pitch-angle diffusion coefficient, D_{pp} is the momentum diffusion coefficient, and $D_{\alpha p} = D_{p\alpha}$ is the mixed diffusion coefficient. The diffusion coefficients depend on the wave spectra and plasma properties. They are generally a function of pitch angle and electron energy.

Following *Liu et al.* [2010], test particle computations are used to investigate the scattering of relativistic electrons by the enhanced fluctuations from the simulated proton Bernstein instability. The test particle code follows the equations of motion of relativistic test electrons in the electric and magnetic fields of input waves which, in the present study, come from the PIC simulation Case I in section 3 during the quasi-steady state (starting from $100\Omega_p^{-1}$). The test particle computation uses the same simulation domain as the PIC simulation ($L_x = 9.6\lambda_i$, $N_x = 128$, $L_y = 64\lambda_i$, and $N_y = 64$) and the realistic electron mass ($m_p/m_e = 1836$). A small time step $\delta t = 1.0 \times 10^{-4}\Omega_p^{-1}$ is employed to well resolve the electron gyro-motion. The test particle computation has 8192 test electrons, enough to make the results statistically significant. The test electrons are initialized to have the same kinetic energy E_e and the same pitch angle α , but have a uniformly-distributed random phase angle ϕ , position x , and position y . *Liu et al.* [2010] showed that $D_{\alpha\alpha}$ can be determined from the slope of the linear temporal growth phase of the mean-square pitch-angle change ($\langle \Delta\alpha^2 \rangle$) of the test electrons

$$D_{\alpha\alpha} = \frac{\langle \Delta\alpha^2 \rangle(t_2) - \langle \Delta\alpha^2 \rangle(t_1)}{2\Delta t}, \quad (5)$$

where $\Delta t = t_2 - t_1$. Similar to the argument in section 2 of *Liu et al.* [2010], one can show that D_{pp} and $D_{\alpha p}$ ($D_{p\alpha}$) can as well be calculated from the linear temporal growth phases of $\langle \Delta p^2 \rangle$ and $\langle \Delta\alpha\Delta p \rangle$, respectively.

The resonance condition for relativistic electron gyroresonant interactions with electromagnetic waves of frequency ω_r and wave number k_{\parallel} is

$$\omega_r - k_{\parallel}v \cos \alpha = n\Omega_e/\gamma, n = 0, \pm 1, \pm 2, \dots \quad (6)$$

At quasi-perpendicular propagation, fast magnetosonic waves have a very small k_{\parallel} . This makes cyclotron resonance ($n \neq 0$) occur only for electrons at very high energy, as discussed in *Horne et al.* [2007]. Consequently, only Landau ($n = 0$) resonance is generally relevant for electrons of 100 keV to several MeV. In the present study, electrons of 500 keV are chosen as an example. To have the electrons in Landau resonance with the strongest wave in the simulation ($\omega_r \approx \Omega_p$, $k_{\perp}\lambda_i \approx 5$, and $k_{\parallel}\lambda_i \approx 0.3$, as shown in Figure 5 and Figure 6), equation (6) requires the initial pitch angle of the electrons to be about 75° . We use this value as the initial pitch angle of the test electrons.

From top to bottom, the three panels of Figure 12 display the time evolutions of $\langle \Delta\alpha^2 \rangle$, $\langle \Delta\alpha\Delta p \rangle / p$, and $\langle \Delta p^2 \rangle / p^2$ of the test electrons, respectively. Similar to the evolution of $\langle \Delta\alpha^2 \rangle$ in electron pitch-angle scattering by electromagnetic ion cyclotron waves [*Liu et al.*, 2010], all three quantities in Figure 12 undergo an initial nonlinear temporal growth phase owing to some coherent factors in the scattering process. When the test particle computation time goes beyond this coherent phase, the three quantities increase linearly in time; later they gradually depart from linear temporal growth when the electrons have significantly diffused from their initial pitch angle and momentum. Using equation (5), the linear temporal growth phase of $\langle \Delta\alpha^2 \rangle$ in the top panel of Figure 12 determines $D_{\alpha\alpha} = 1.6 \times 10^{-3}\Omega_p$. Similarly, $D_{\alpha p}/p = D_{p\alpha}/p = 4.3 \times 10^{-4}\Omega_p$ and $D_{pp}/p^2 = 1.2 \times 10^{-4}\Omega_p$ are calculated from the linear temporal growth phases of $\langle \Delta\alpha\Delta p \rangle / p$, and $\langle \Delta p^2 \rangle / p^2$. For Landau resonance, quasi-linear theory predicts

that $D_{\alpha\alpha}/(D_{\alpha p}/p) = (D_{\alpha p}/p)/(D_{pp}/p^2) = -\sin\alpha/\cos\alpha$ [Lyons, 1974]. The diffusion coefficients derived from Figure 12 follow this relation nicely. In addition, quasi-linear theory estimates $D_{\alpha\alpha} \approx 2 \times 10^{-3}\Omega_p$ (Appendix), which is close to the one calculated from Figure 12. As in Horne *et al.* [2007], even though $D_{\alpha\alpha}$ is larger than D_{pp}/p^2 , because the resonant electrons have $\alpha = 75^\circ$, which is far away from the loss cone, the net effect of these waves is to energize the electrons, rather than scatter them into the loss cone.

6. Summary and Discussion

The general properties of an ion Bernstein instability driven by a proton velocity distribution with positive slope in $f_p(v_\perp)$ are studied using linear kinetic dispersion theory and two-dimensional electromagnetic PIC simulations. A simple subtracted Maxwellian distribution is first used to construct the positive slope in $f_p(v_\perp)$ in the present study because our linear kinetic dispersion code is based on bi-Maxwellian velocity distributions. The results of a simulation using such an initial proton distribution agree well with the linear kinetic analysis. The distribution in the simulation is further generalized to contain a proton shell (at twice the Alfvén velocity) with a finite thermal spread and a relatively cold ion background (90%). The simulation results show that the presence of the cold background protons and the increase of the shell velocity shift the excited waves close to the cold plasma dispersion relation for magnetosonic waves ($\omega_r = kv_A$). This trend is consistent with the simple theoretical model in Perraut *et al.* [1982].

The present results also demonstrate that the ion Bernstein instability grows at propagation angles nearly perpendicular to \mathbf{B}_0 , saturates at a very low level, and yields spectral peaks at frequencies close to the first few harmonics of the proton cyclotron frequency. These general features resemble the observed fast magnetosonic waves in different regions

of the magnetosphere. The simulation using the subtracted Maxwellian distribution represents a region when the presence of the relatively cold background ions is not significant and the shell (ring) velocity is relatively small. The excited waves are essentially the ion Bernstein waves studied in *Denton et al.* [2010] and *Gary et al.* [2010] and have been observed in the plasma sheet boundary layer [*Engbreton et al.*, 2010]. This case may also apply to the nightside of the inner magnetosphere in the injection region as discussed in *Perraut et al.* [1982]. On the other hand, the simulation using the generalized proton distribution represents a case when the presence of the background ions is significant and the shell (ring) velocity is large. The excited waves approximately follow the cold plasma dispersion relation for magnetosonic waves. This case is more typical to the inner magnetosphere, especially inside the plasmasphere.

Limited by the computational resources available, a reduced proton-to-electron mass ratio and a relatively small ω_p/Ω_p are used in the present simulations. As discussed in section 2, choosing such reduced parameters slightly affects the properties of the ion Bernstein instability, but does not change the essential physics. However, the reduced parameters lower the lower hybrid frequency to about $8\Omega_p$. This limits the excited waves to the first few proton cyclotron harmonics, while some observations [*Boardsen et al.*, 1992] and linear theories [*Gul’elmi et al.*, 1975; *Horne et al.*, 2000] show spectra which peak at higher harmonics of the proton cyclotron frequency. Our current linear kinetic dispersion code is based on bi-Maxwellian velocity distributions and only applies to the subtracted Maxwellian distribution case. Since $n_2/n_1 < (T_2/T_1)^{3/2}$ is required in equation (1) to avoid negative values of $f_p(v)$, only moderately positive slopes in $f_p(v_\perp)$ can be used and the shell velocity cannot be easily adjusted without affecting the thermal spread of

the shell. Linear kinetic dispersion analysis for the generalized proton distribution should be carried out so the effect of the shell proton density, the shell velocity, the thermal spread of the shell, the temperature of the background ions, and the temperature of the electrons on the instability can be comprehensively investigated. Such an analysis could be used to demonstrate how the instability changes from being “ion Bernstein”-like (in the sense of *Denton et al.* [2010] and *Gary et al.* [2010]) to more “magnetosonic”-like (in the usual sense) as the parameters of the ion distribution are varied.

Finally, a test particle computation using the simulated electromagnetic fluctuations suggests that this growing mode may play an important role in the acceleration of radiation-belt electrons. The enhanced electromagnetic waves pitch-angle scatter and also accelerate the relativistic electrons. The calculated diffusion coefficients from the test particle computation show good agreement with quasi-linear theory.

Appendix A: Quasi-linear Diffusion Coefficients

Equation (5) of *Lyons* [1974] gives the non-relativistic pitch-angle diffusion coefficient in quasi-linear theory,

$$D_{\alpha\alpha}^* = \sum_{n=-\infty}^{\infty} \int_0^{\infty} k_{\perp} dk_{\perp} D_{\alpha\alpha}^{nk_{\perp}}, \quad (\text{A1})$$

where

$$D_{\alpha\alpha}^{nk_{\perp}} = \lim_{V \rightarrow \infty} \frac{\pi q^2}{(2\pi)^2 V m^2} \left(\frac{-\sin^2 \alpha + n\Omega/\omega_{\mathbf{k}}}{\cos \alpha} \right)^2 \frac{|\theta_{n\mathbf{k}}|^2}{|v_{\parallel} - \partial\omega_{\mathbf{k}}/\partial k_{\parallel}|} \Big|_{k_{\parallel}=k_{\parallel, \text{res}}}, \quad (\text{A2})$$

$$\theta_{n\mathbf{k}} = \frac{E_{\mathbf{k},R} J_{n+1} + E_{\mathbf{k},L} J_{n-1}}{\sqrt{2}} + \frac{v_{\parallel}}{v_{\perp}} E_{\mathbf{k},\parallel} J_n, \quad (\text{A3})$$

$E_{\mathbf{k},R} = (E_{\mathbf{k},x} - iE_{\mathbf{k},y})/\sqrt{2}$, $E_{\mathbf{k},L} = (E_{\mathbf{k},x} + iE_{\mathbf{k},y})/\sqrt{2}$ (the background magnetic field is in the z direction in *Lyons* [1974]), the argument of the Bessel functions is $k_{\perp} v_{\perp}/\Omega$, V is

the plasma volume, $\omega_{\mathbf{k}}$ is the wave frequency as a function of the wave vector \mathbf{k} , q is the particle charge of a plasma species, m is its rest mass, and Ω is its cyclotron frequency.

The dimensions of the diffusion coefficients in *Lyons* [1974] are different with the ones in equation (4), so a superscript $*$ has been used in equation (A1) to distinguish the difference, $D_{\alpha\alpha} = D_{\alpha\alpha}^*/p^2$ [*Summers*, 2005]. *Lyons* [1974] also stated that equations (A1) to (A3) can be generalized to include relativistic effects if Ω is replaced by Ω/γ , and $D_{\alpha\alpha}^{nk_{\perp}}$ is multiplied by m^2 . After taking all of these into consideration, the general expression of the relativistic version of $D_{\alpha\alpha}$ is,

$$D_{\alpha\alpha} = \frac{\pi q^2}{p^2} \sum_{n=-\infty}^{\infty} \lim_{V \rightarrow \infty} \int \frac{d^3\mathbf{k}}{(2\pi)^3 V} \left(\frac{-\sin^2 \alpha + n\Omega/\gamma\omega_{\mathbf{k}}}{\cos \alpha} \right)^2 \cdot \delta(k_{\parallel}v_{\parallel} + n\Omega/\gamma - \omega_{\mathbf{k}}) |\theta_{n\mathbf{k}}|^2, \quad (\text{A4})$$

with the argument of the Bessel functions in $\theta_{n\mathbf{k}}$ being $\gamma k_{\perp} v_{\perp} / \Omega$.

For field-aligned transverse plasma waves, $k_{\perp} = 0$ and $E_{\parallel} = 0$. Using the property that all Bessel functions with zero argument vanish except $J_0(0) = 1$, we write Equation (A4) as

$$D_{\alpha\alpha} = \frac{\pi c^2 \Omega^2}{2\gamma^2 v^2 W_0} \int_{-\infty}^{\infty} dk_{\parallel} \left[\left(\frac{-\sin^2 \alpha - \Omega/\gamma\omega_{\mathbf{k}}}{\cos \alpha} \right)^2 \delta(k_{\parallel}v_{\parallel} - \Omega/\gamma - \omega_{\mathbf{k}}) W_{E_R}(k_{\parallel}) + \left(\frac{-\sin^2 \alpha + \Omega/\gamma\omega_{\mathbf{k}}}{\cos \alpha} \right)^2 \delta(k_{\parallel}v_{\parallel} + \Omega/\gamma - \omega_{\mathbf{k}}) W_{E_L}(k_{\parallel}) \right], \quad (\text{A5})$$

where $W_0 = B_0^2/2\mu_0$ is the energy density of the background magnetic field, $W_{E_R}(k_{\parallel})$ and $W_{E_L}(k_{\parallel})$ are the wave energy spectral densities of E_R and E_L , respectively. Here we have also used

$$\frac{\epsilon_0}{2} \lim_{V \rightarrow \infty} \int \frac{d^3\mathbf{k}}{(2\pi)^3 V} |E_{\mathbf{k}}|^2 = \int_{-\infty}^{\infty} dk_{\parallel} W_E(k_{\parallel}). \quad (\text{A6})$$

Using the relation that $W_E(k_{\parallel}) = (\omega/k_{\parallel}c)^2 W_B(k_{\parallel})$, one can easily obtain the expression for $D_{\alpha\alpha}$ in *Summers* [2005] (equations (17) and (27)). *Albert* [2007] noticed that equation

(1) in *Summers* [2005] has an extra factor of 2, which is not apparent in earlier work of quasi-linear theory, e.g., equation (1) of *Lyons* [1974]. However, $E_{\mathbf{k},R} = E_{\mathbf{k},x} - iE_{\mathbf{k},y}$ and $E_{\mathbf{k},L} = E_{\mathbf{k},x} + iE_{\mathbf{k},y}$ in *Summers* [2005], which are different with the definitions in *Lyons* [1974]. Consequently, there is a factor of 2 missing in equation (11) of *Summers* [2005] which relates the integral in equation (A4) to the wave energy spectral density. The omitting of 2 in equation (11) of *Summers* [2005] cancels the extra factor of 2 in equation (1) and makes the final diffusion coefficient expressions exact (equations (17) to (19)).

As discussed in *Horne et al.* [2007], only Landau ($n = 0$) resonance is generally relevant for electrons scattering by quasi-perpendicular propagating fast magnetosonic waves. So

$$\begin{aligned}\theta_{0\mathbf{k}} &= \frac{E_{\mathbf{k},R}J_1 + E_{\mathbf{k},L}J_{-1}}{\sqrt{2}} + \frac{v_{\parallel}}{v_{\perp}}E_{\mathbf{k},\parallel}J_0 \\ &= -iE_{\mathbf{k},y}J_1 + \frac{v_{\parallel}}{v_{\perp}}E_{\mathbf{k},\parallel}J_0,\end{aligned}\tag{A7}$$

where $J_1 = -J_{-1}$ has been used.

For the spectral peak at $k_{\perp}\lambda_i \approx 5$ and $k_{\parallel}\lambda_i \approx 0.3$ in Figure 5, the argument of the Bessel functions in $\theta_{n\mathbf{k}}$ is $\gamma k_{\perp}v_{\perp}/\Omega = 0.07$ for electrons of 500 keV and $\alpha = 75^\circ$. So $J_1 \ll J_0 \approx 1$. The PIC simulation domain in the present study is two-dimensional and the background magnetic field is in the y direction, so $E_{\mathbf{k},\parallel}$ and $E_{\mathbf{k},y}$ in equation (A7) correspond to E_y and $-E_z$ in the simulation, respectively. Figure 4 then shows that $E_{\mathbf{k},\parallel}$ is only slightly less than $E_{\mathbf{k},y}$. Consequently, $\theta_{0\mathbf{k}} \approx 0.3E_{\mathbf{k},\parallel}$, and

$$\begin{aligned}D_{\alpha\alpha} &= \frac{\pi q^2}{p^2} \lim_{V \rightarrow \infty} \int \frac{d^3\mathbf{k}}{(2\pi)^3V} \left(\frac{\sin^2 \alpha}{\cos \alpha} \right)^2 \delta(k_{\parallel}v_{\parallel} - \omega_{\mathbf{k}}) |0.3E_{\mathbf{k},\parallel}|^2 \\ &= \frac{2 \times 0.09\pi q^2}{\epsilon_0 p^2} \left(\frac{\sin^2 \alpha}{\cos \alpha} \right)^2 \int_{-\infty}^{\infty} dk_x \int_{-\infty}^{\infty} dk_{\parallel} \delta(k_{\parallel}v_{\parallel} - \omega_{\mathbf{k}}) W_{E_{\parallel}}(k_x, k_{\parallel}) \\ &= \frac{0.09\pi c^2 \Omega^2}{\gamma^2 v^2 W_0} \left(\frac{\sin^2 \alpha}{\cos \alpha} \right)^2 \sum_j \int_{-\infty}^{\infty} dk_x \frac{W_{E_{\parallel}}(k_x, k_{\parallel})}{|v_{\parallel} - \partial\omega_{\mathbf{k}}/\partial k_{\parallel}|} \Big|_{k_{\parallel}=k_{\parallel, res}},\end{aligned}\tag{A8}$$

where the sum is performed over all roots ($k_{\parallel, res}$) of the resonance condition ($k_{\parallel}v_{\parallel} - \omega_{\mathbf{k}} = 0$), $W_{E_{\parallel}}(k_x, k_{\parallel})$ is the wave energy spectral density of E_{\parallel} from the two-dimensional PIC simulation and

$$\frac{\epsilon_0}{2} \lim_{V \rightarrow \infty} \int \frac{d^3\mathbf{k}}{(2\pi)^3 V} |E_{\mathbf{k}, \parallel}|^2 = \int_{-\infty}^{\infty} dk_x \int_{-\infty}^{\infty} dk_{\parallel} W_{E_{\parallel}}(k_x, k_{\parallel}). \quad (\text{A9})$$

As shown in Figure 5, the spectral peak is relatively narrow in k_x . We may further approximate equation (A8) to,

$$D_{\alpha\alpha} = \frac{0.09\pi c^2 \Omega^2}{\gamma^2 v^2 W_0} \left(\frac{\sin^2 \alpha}{\cos \alpha} \right)^2 \frac{\Delta k_x W_{E_{\parallel}}(k_x, k_{\parallel})}{|v_{\parallel} - \partial\omega_{\mathbf{k}}/\partial k_{\parallel}|} \bigg|_{k_{\parallel}=k_{\parallel, res}}. \quad (\text{A10})$$

With $\Delta k_x \lambda_i \approx 0.5$, $W_{E_{\parallel}}(k_x, k_{\parallel}) \approx 1 \times 10^{-9}$ ($W_0 = 1$, E has been normalized to cB_0 and k is normalized to λ_i) from the simulation and $\partial\omega_{\mathbf{k}}/\partial k_{\parallel} \approx 2v_A$ from the linear kinetic analysis, equation (A10) gives $D_{\alpha\alpha} \approx 2 \times 10^{-3} \Omega_p$, which is close to the one derived from the test particle computation in section 5.

Acknowledgments. This work was performed under the auspices of the U.S. Department of Energy (DOE). It was supported primarily by the Defense Threat Reduction Agency under the “Basic Research for Combating Weapons of Mass Destruction (WMD)” Program, project IACRO # 07-4323I, with additional support from the Heliospheric Guest Investigators Program of the National Aeronautics and Space Administration. This research was also conducted as part of the Dynamic Radiation Environment Assimilation Model (DREAM) project at Los Alamos National Laboratory. We are grateful to the sponsors of DREAM for financial and technical support. Computational resources supporting this work were provided by the NASA High-End Computing (HEC) Program through the NASA Advanced Supercomputing (NAS) Division at Ames Research Center.

References

- Albert, J. M. (2007), Simple approximations of quasi-linear diffusion coefficients, *J. Geophys. Res.*, *112*, A12202, doi:10.1029/2007JA012551.
- Ashour-Abdalla, M., J. N. Leboeuf, D. Schriver, J.-M. Bosqued, N. Cornilleau-Wehrlin, V. Sotnikov, A. Marchaudon, and A. N. Fazakerley (2006), Instabilities driven by ion shell distributions observed by Cluster in the midaltitude plasma sheet boundary layer, *J. Geophys. Res.*, *111*, A10223, doi:10.1029/2005JA011490.
- Boardsen, S., D. Gallagher, D. Gurnett, W. Peterson, and J. Green (1992), Funnel-shaped, low-frequency equatorial waves, *J. Geophys. Res.*, *97*(A10), 14,967.
- Bortnik, J., and R. M. Thorne (2010), Transit-time scattering of energetic electrons due to equatorially-confined magnetosonic waves, *J. Geophys. Res.*, *115*, A07213, doi:10.1029/2010JA015283.
- Chen, L., R. M. Thorne, V. K. Jordanova, and R. B. Horne (2010), Global simulation of magnetosonic wave instability in the storm time magnetosphere, *J. Geophys. Res.*, *115*, A11222, doi:10.1029/2010JA015707.
- Curtis, S. A. (1985), Equatorial trapped plasmasphere ion distributions and transverse stochastic acceleration, *J. Geophys. Res.*, *90*(A2), 1765.
- Denton, R. E., M. J. Engebretson, A. Keiling, A. P. Walsh, S. P. Gary, P. M. E. Décréau, C. A. Cattell, K.-H. Glassmeier, and H. Rème (2010), Multiple harmonic ULF waves in the plasma sheet boundary layer: Instability analysis, *J. Geophys. Res.*, doi:10.1029/2010JA015928, in press.
- Engebretson, M. J., C. R. G. Kahlstorf, J. L. Posch, A. Keiling, A. P. Walsh, R. E. Denton, M. C. Broughton, C. J. Owen, K.-H. Fornacon, and H. Réme (2010), Multiple harmonic

- 534 ULF waves in the plasma sheet boundary layer observed by cluster, *J. Geophys. Res.*,
535 doi:10.1029/2010JA015929, in press.
- 536 Gary, S. P. (1993), *Theory of space plasma microinstabilities*, Cambridge Univ. Press,
537 New York.
- 538 Gary, S. P., K. Liu, D. Winske, and R. E. Denton (2010), Ion Bernstein instability in
539 the terrestrial magnetosphere: Linear dispersion theory, *J. Geophys. Res.*, *115*, A12209,
540 doi:10.1029/2010JA015965.
- 541 Gul’elmi, A. V., B. I. Klaine, and A. S. Potapov (1975), Excitation of magnetosonic waves
542 with discrete spectrum in the equatorial vicinity of the plasmopause, *Planet. Space Sci.*,
543 *23*, 279.
- 544 Horne, R., G. Wheeler, and H. Alleyne (2000), Proton and electron heating by radially
545 propagating fast magnetosonic waves, *J Geophys Res*, *105*, A12.
- 546 Horne, R. B., and R. M. Thorne (1998), Potential waves for relativistic electron scattering
547 and stochastic acceleration during magnetic storms, *Geophys. Res. Lett.*, *25*(15), 3011.
- 548 Horne, R. B., R. M. Thorne, S. A. Glauert, N. P. Meredith, D. Pokhotelov, and O. Santolík
549 (2007), Electron acceleration in the van allen radiation belts by fast magnetosonic waves,
550 *Geophys. Res. Lett.*, *34*, L17107, doi:10.1029/2007GL030267.
- 551 Janhunen, P., A. Olsson, A. Vaivads, and W. K. Peterson (2003), Generation of Bernstein
552 waves by ion shell distributions in the auroral region, *Ann. Geophys.*, *21*(4), 881.
- 553 Kennel, C. F., and F. Engelmann (1966), Velocity space diffusion from weak plasma
554 turbulence in a magnetic field, *Phys. Fluids*, *9*(12), 2377.
- 555 Lee, J. K., and C. K. Birdsall (1979), Velocity space ring-plasma instability, magnetized,
556 part ii: Simulation, *Phys. Fluids*, *22*(7), 1315.

- 557 Lerche, I. (1968), Quasilinear theory of resonant diffusion in a magneto-active, relativistic
558 plasma, *Phys. Fluids*, *11*(8), 1720.
- 559 Liu, K., C. E. Seyler, and T. Xu (2006), Particle-in-cell simulations of current shear-
560 driven instabilities and the generation of broadband ELF fluctuations, *J Geophys Res*,
561 *111*, A11307, doi:10.1029/2006JA011858.
- 562 Liu, K., D. S. Lemons, D. Winske, and S. P. Gary (2010), Relativistic electron scattering
563 by electromagnetic ion cyclotron fluctuations: Test particle simulations, *J Geophys Res*,
564 *115*, A04204, doi:10.1029/2009JA014807.
- 565 Lyons, L. R. (1974), General relations for resonant particle diffusion in pitch angle and
566 energy, *J. Plasma Phys.*, *12*, 45.
- 567 McClements, K., R. Dendy, and C. Lashmore-Davies (1994), A model for the genera-
568 tion of obliquely propagating ULF waves near the magnetic equator, *J. Geophys. Res.*,
569 *99*(A12), 23,685.
- 570 Meredith, N. P., R. B. Horne, and R. R. Anderson (2008), Survey of magnetosonic waves
571 and proton ring distributions in the Earth's inner magnetosphere, *J Geophys Res*, *113*,
572 A06213, doi:10.1029/2007JA012975.
- 573 Perraut, S., A. Roux, P. Robert, R. Gendrin, J.-A. Sauvaud, J.-M. Bosqued, G. Kremser,
574 and A. Korth (1982), A systematic study of ULF waves above F_{H+} from GEOS 1 and 2
575 measurements and their relationships with proton ring distributions, *J. Geophys. Res.*,
576 *87*(A8), 6219.
- 577 Russell, C., R. Holzer, and E. Smith (1970), OGO 3 observations of ELF noise in the
578 magnetosphere, 2. the nature of the equatorial noise, *J. Geophys. Res.*, *75*(4), 755.

- Santolík, O., J. S. Pickett, D. A. Gurnett, M. Maksimovic, and N. Cornilleau-Wehrin
(2002), Spatiotemporal variability and propagation of equatorial noise observed by cluster, *J. Geophys. Res.*, *107*(A12), 1495, doi:10.1029/2001JA009159.
- Seyler, C. E., and K. Liu (2007), Particle energization by oblique inertial alfvén waves in the auroral region, *J. Geophys. Res.*, *112*, A09302, doi:10.1029/2007JA012412.
- Shprits, Y. Y. (2009), Potential waves for pitch-angle scattering of near-equatorially mirroring energetic electrons due to the violation of the second adiabatic invariant, *Geophys. Res. Lett.*, *36*, L12106, doi:10.1029/2009GL038322.
- Summers, D. (2005), Quasi-linear diffusion coefficients for field-aligned electromagnetic waves with applications to the magnetosphere, *J. Geophys. Res.*, *110*(A08213), doi:10.1029/2005JA011159.

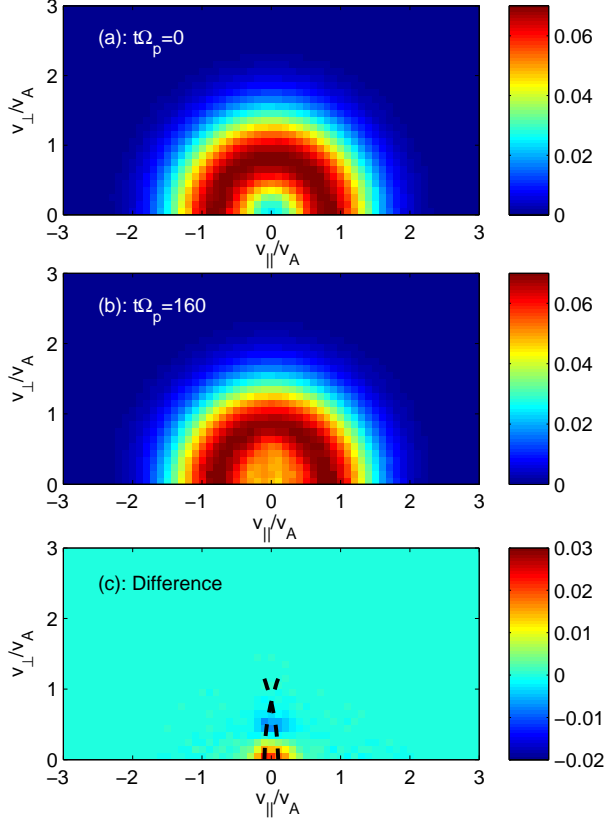


Figure 1. The proton velocity distributions in the v_{\parallel} - v_{\perp} coordinates ($f_p(v_{\perp}, v_{\parallel})$). (a) The proton velocity distribution given by equation (1), which is used in the linear kinetic dispersion analysis of section 2 and as an initial condition in simulation Case I of section 3. (b) The proton velocity distribution at $t\Omega_p = 160$ from simulation Case I of section 3. (c) The difference between (a) and (b). It highlights the change of the proton distribution from $t\Omega_p = 0$ to $t\Omega_p = 160$ in simulation Case I. The two dashed lines represent the diffusion surfaces for protons of $v_{\parallel} = 0$ and $v_{\perp}/v_A = 0.8$ interacting with the strongest waves in the simulation as described in section 3.

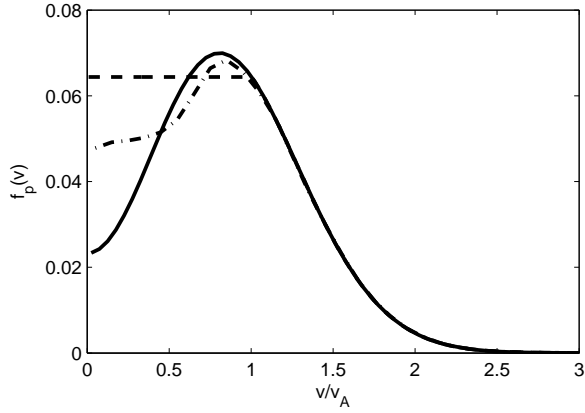


Figure 2. The proton velocity distributions. The solid line represents the subtracted Maxwellian proton velocity distribution given by equation (1), which is used in the linear kinetic dispersion analysis of section 2 and as an initial condition in simulation Case I of section 3. The dashed line stands for the closest equilibrium distribution corresponding to the solid line as defined in the text. The dash-dotted line displays $f_p(v_\perp)$ for protons of $|v_\parallel|/v_A \leq 0.01$ at $t\Omega_p = 160$ from simulation Case I of section 3. The three lines overlay on each other after $v/v_A \approx 1$.

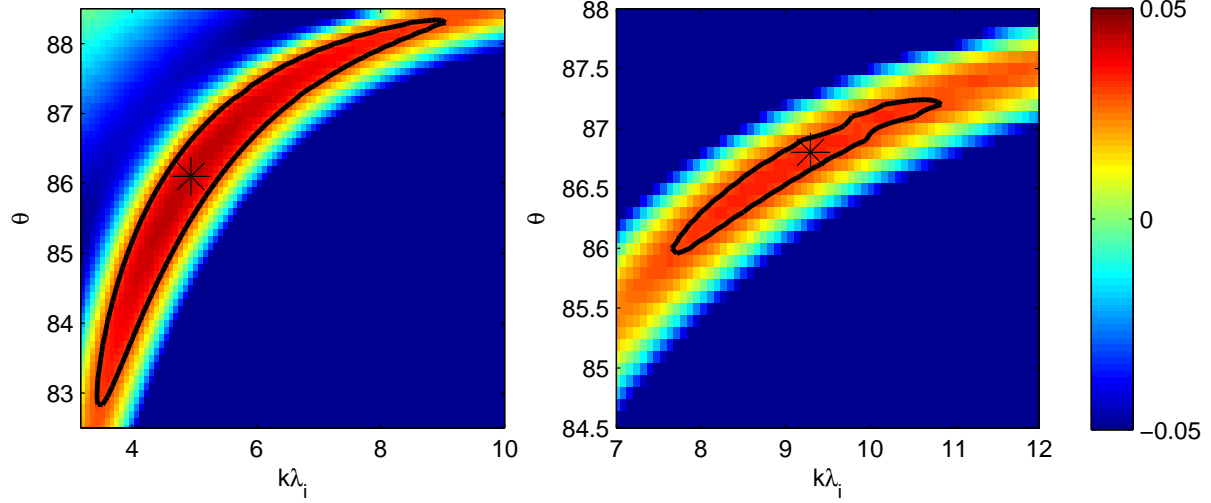


Figure 3. Linear dispersion theory results: Growth rates as a function of $k\lambda_i$ and propagation angle θ (with regard to \mathbf{B}_0) for waves near the first (left panel) and the second (right panel) proton cyclotron harmonics. The asterisk in each panel represents the location of the local maximum growth rate. The solid black contour line in each panel represents the contour of $\gamma/\Omega_p = 0.03$. Note that the minimum value of the color scale corresponds to $\gamma/\Omega_p = -0.05$ so larger damping rates saturate in the plot.

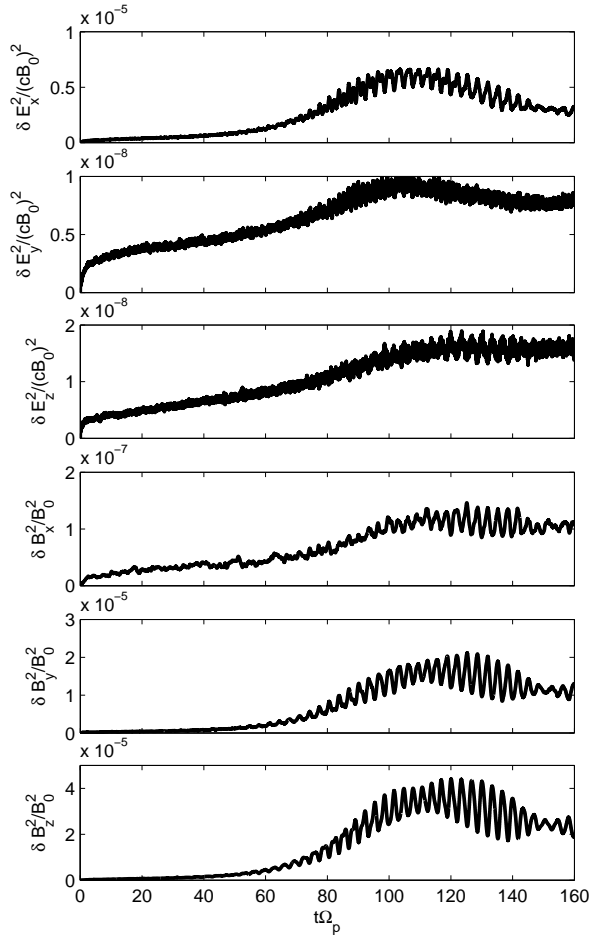


Figure 4. Simulation Case I: The time evolution of the energies in different electric and magnetic field components. The panels from top to bottom are for E_x , E_y , E_z , B_x , B_y , and B_z , respectively.

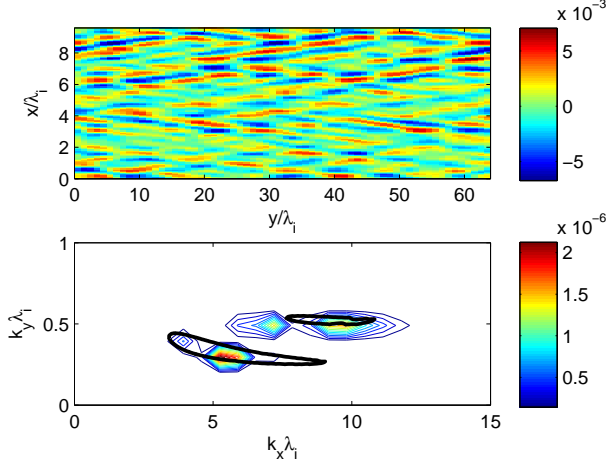


Figure 5. Simulation Case I: The E_x fluctuations at $t\Omega_p = 120$. Top panel: The contour plot of E_x/cB_0 . Bottom panel: The spatial power spectrum of E_x/cB_0 . The two solid black contour lines in the bottom panel are the same ones in Figure 3 but are now plotted in the $k_\perp \lambda_i$ - $k_\parallel \lambda_i$ coordinates. They represent the contours of $\gamma/\Omega_p = 0.03$ given by linear kinetic dispersion theory for waves near the first two proton cyclotron harmonics. The lower left contour is for the first harmonic while the upper right contour is for the second harmonic.

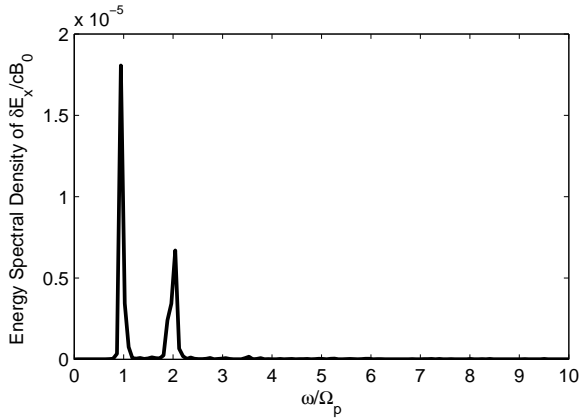


Figure 6. Simulation Case I: The temporal spectrum of E_x at $x = 4.8\lambda_i$ and $y = 32\lambda_i$ from $t\Omega_p = 80$ to $t\Omega_p = 160$.

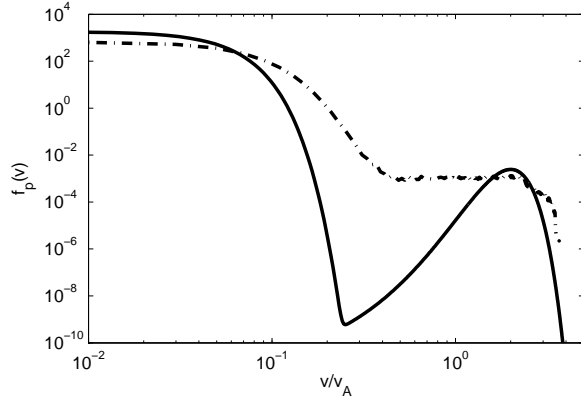


Figure 7. The proton velocity distributions in simulation Case II. The solid line represents the initial distribution given by equation (3) with $n_s/n_0 = 0.1$, $v_{sth}/v_A = 0.45$, $v_s/v_A = 2.0$, $n_b/n_0 = 0.9$ and $v_{bth}/v_A = 0.045$. The dash-dotted line displays $f_p(v_\perp)$ for protons of $|v_\parallel|/v_A \leq 0.02$ at $t\Omega_p = 100$ from the simulation.

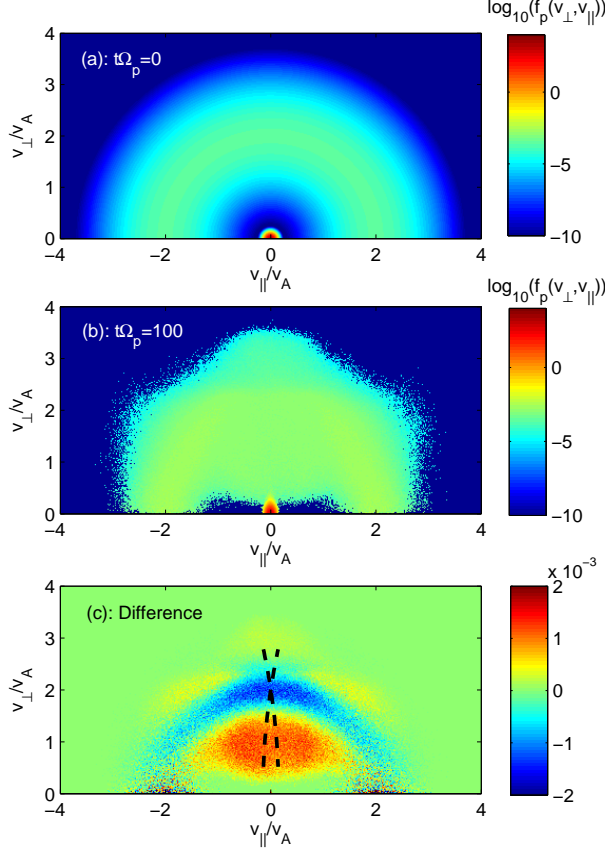


Figure 8. The proton velocity distributions in the v_{\parallel} - v_{\perp} coordinates ($f_p(v_{\perp}, v_{\parallel})$) in simulation Case II. (a) The initial proton velocity distribution given by equation (3) with $n_s/n_0 = 0.1$, $v_{sth}/v_A = 0.45$, $v_s/v_A = 2.0$, $n_b/n_0 = 0.9$ and $v_{bth}/v_A = 0.045$. (b) The proton velocity distribution at $t\Omega_p = 100$ from the simulation. (c) The change of the shell proton distribution from $t\Omega_p = 0$ to $t\Omega_p = 100$ in the simulation. The two dashed lines represent the diffusion surfaces for protons of $v_{\parallel} = 0$ and $v_{\perp}/v_A = 2$ interacting with the strongest waves in the simulation as described in the text. Note the color scales in panels (a) and (b) display $f_p(v_{\perp}, v_{\parallel})$ in logarithmic scale while the color scale in panel (c) is linear.

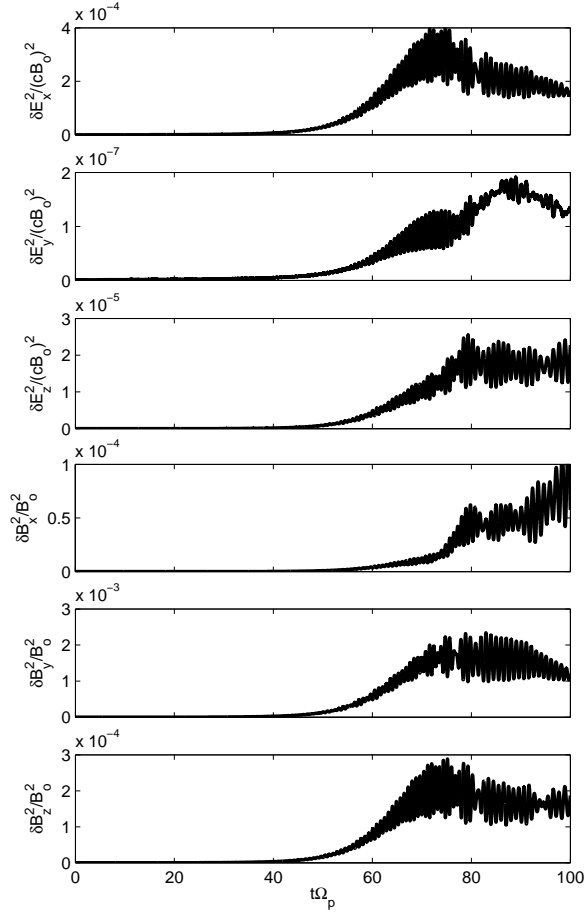


Figure 9. Simulation Case II: The time evolution of the energies in different electric and magnetic field components. The panels from top to bottom are for E_x , E_y , E_z , B_x , B_y , and B_z , respectively.

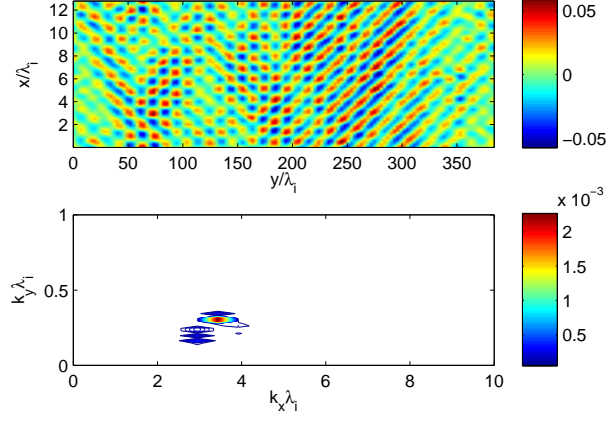


Figure 10. Simulation Case II: The E_x fluctuations at $t\Omega_p = 70$. Top panel: The contour plot of E_x/cB_0 . Bottom panel: The spatial power spectrum of E_x/cB_0 .

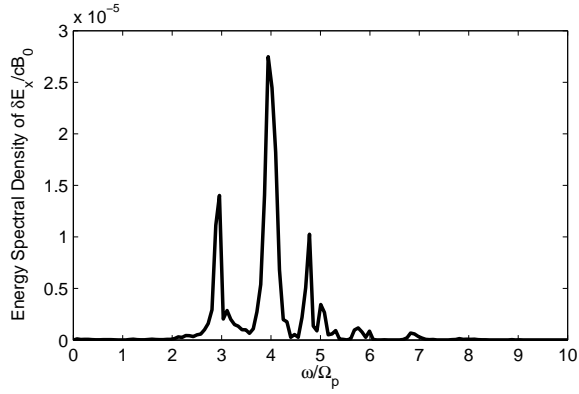


Figure 11. Simulation Case II: The temporal spectrum of E_x/cB_0 at $x = 6.4\lambda_i$ and $y = 192\lambda_i$ from $t\Omega_p = 0$ to $t\Omega_p = 100$.

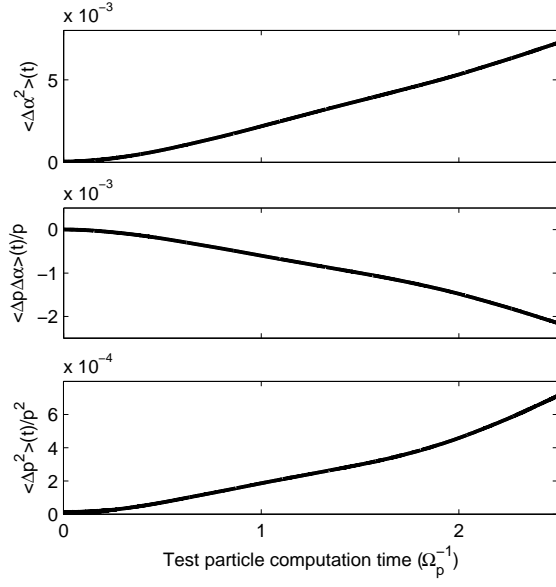


Figure 12. The time evolutions of $\langle \Delta \alpha^2 \rangle$ (top), $\langle \Delta \alpha \Delta p \rangle / p$ (middle), and $\langle \Delta p^2 \rangle / p^2$ (bottom) of the test electrons of 500 keV and $\alpha = 75^\circ$ in the test particle computation.